The Astrophysical Journal, 864:118 (9pp), 2018 September 10 https://doi.org/10.3847/1538-4357/aad6e3

Evidence of Jet–Clump Interaction: A Flip of the Radio Jet Head of 3C 84

M. Kino[1,2], K. Wajima[3], N. Kawakatu[4], H. Nagai[2], M. Orienti[5], G. Giovannini[5,6], K. Hada[2], K. Niinuma[7], and M. Giroletti[5]
[1] Kogakuin University of Technology & Engineering, Academic Support Center, 2665-1 Nakano, Hachioji, Tokyo 192-0015, Japan; motoki.kino@nao.ac.jp
[2] National Astronomical Observatory of Japan, 2-21-1 Osawa, Mitaka, Tokyo, 181-8588, Japan
[3] Korea Astronomy and Space Science Institute, 776 Daedeokdae-ro, Yuseong-gu, Daejeon 34055, Republic of Korea
[4] National Institute of Technology, Kure College, 2-2-11, Agaminami, Kure, Hiroshima, 737-8506, Japan
[5] INAF—Istituto di Radioastronomia, via Gobetti 101, I-40129 Bologna, Italy
[6] Dipartimento di Astronomia, Universita' di Bologna, via Gobetti 103/2, I-40129, Bologna, Italy
[7] Graduate School of Sciences and Technology for Innovation, Yamaguchi University, 1677-1 Yoshida, Yamaguchi, Yamaguchi 753-8512, Japan
Received 2018 March 5; revised 2018 July 24; accepted 2018 July 28; published 2018 September 5

Abstract

Radio jets in active galaxies have been expected to interact with circumnuclear environments in their early phase evolutions. By performing the multi-epoch monitoring observation with the KVN and VERA Array at 43 GHz, we investigate the kinematics of the notable newborn bright component C3 located at the tip of the recurrent jet of 3C 84. During 2015 August–September, we discover the flip of C3 and the amount of the flip is about 0.4 mas in angular scale, which corresponds to 0.14 parsec in physical scale. After the flip of C3, it wobbled at the same location for a few months and then it restarted to propagate toward the southern direction. The flux density of C3 coherently showed the monotonic increase during the observation period. The flip is in good agreement with hydrodynamical simulations of jets in clumpy ambient medium. We estimate the number density of the putative clump based on the momentum balance between the jet thrust and the ram pressure from the clump and it is about 10^{3-5} cm^{-3}. We briefly discuss possible origins of the clump.

Key words: galaxies: active – galaxies: individual (3C 84, NGC 1275) – gamma rays: galaxies – radio continuum: galaxies

1. Introduction

Active galactic nuclei (AGNs) are powered by surrounding gas accretion onto supermassive black holes (BHs) at the center of each galaxy. Since the circumnuclear material plays important roles of a gas reservoir for the accretion flow, its nature, such as the structure, the size, and the mass, has been intensively investigated (e.g., Ramos Almeida & Ricci 2017 for review). While AGNs themselves radiate across the entire electromagnetic spectrum, from the radio and up to γ-rays, circumnuclear material do not emit significant electromagnetic signal. Hence, circumnuclear matter distributions in particular at the central parsec-scale regions in AGNs are highly uncertain. Observationally, there are some indications of inhomogeneous matter distribution. Very Long Baseline Interferometer (VLBI) observations of young radio sources reveal that a large fraction of young radio lobes with a two-sided structure show an asymmetry in arm-length ratio and their flux density from a pair of the lobes, and the pair of lobes satisfies a brighter-when-farther behavior (Dallacasa et al. 2013; Orienti & Dallacasa 2014; Orienti 2016). This asymmetry can be naturally explained by the interaction between the jet and an inhomogeneous environment. At the X-ray energy band, time variations in absorbing column density on timescales from months to years have been known, which indicate highly non-uniform circumnuclear material such as clumps on a sub-parsec scale (Ives et al. 1976; Malizia et al. 1997; Risaliti et al. 2002). Theoretically, jets are thought to have a strong impact on the interstellar medium (ISM) of a host radio galaxy. The deposition of jet mechanical energy may affect the formation of stars in the host galaxy and the accretion of matter down the gravitational potential onto the central BH, which is so-called AGN feedback (e.g., Silk & Rees 1998; Bicknell et al. 2000; King 2003; Croton et al. 2006; Fabian 2012). In the context of AGN feedback, Wagner & Bicknell (2011) ran numerical simulations of AGN jets interacting with a non-uniform medium containing dense clumps, focusing on the effects of the AGN jet on the cold dense clumps in which stars were formed. Intriguingly, Wagner & Bicknell (2011) indicated flips of the jet-head were caused by the interaction with the clumps, although such a phenomenon has not yet been observed so far. Similar behaviors have been also reported in several other studies (e.g., Fragile et al. 2017). However, no direct observational evidence of this impact has been reported so far.

NGC 1275 is a notable nearby giant elliptical galaxy at the core of the Perseus cluster, with an optically luminous nucleus, currently classified as a Seyfert 1.5/LINER (Sosa-Brito et al. 2001). Interestingly, Nagai et al. (2010) found the emergence of a newborn bright component, designated C3, during multi-epoch monitoring of 3C 84 using VLBI. C3 showed a proper motion toward the southern direction with an apparent velocity of 0.2–0.3 c (Nagai et al. 2010; Suzuki et al. 2012; Hiura et al. 2018). Since various observations of 3C 84 indicate a gas-rich environment such with molecular gas (Krabbe et al. 2000; Salomé et al. 2006; Lim et al. 2008), warm [H_2] gas (Wilman et al. 2005; Scharwächter et al. 2013) and dense ionized plasma surrounding the 3C 84 jet (O'Dea et al. 1984; Walker et al. 2000), 3C 84 is regarded as a quite unique laboratory to explore interactions between the jet and the circumnuclear environment on parsec scales. In this work, we will report the KVN and VERA Array (KaVA) monitoring observations of 3C 84 during 2015–2016, in which we indeed discover the theoretically predicted flip of the jet-head accompanying a clear increase of the C3 flux density.

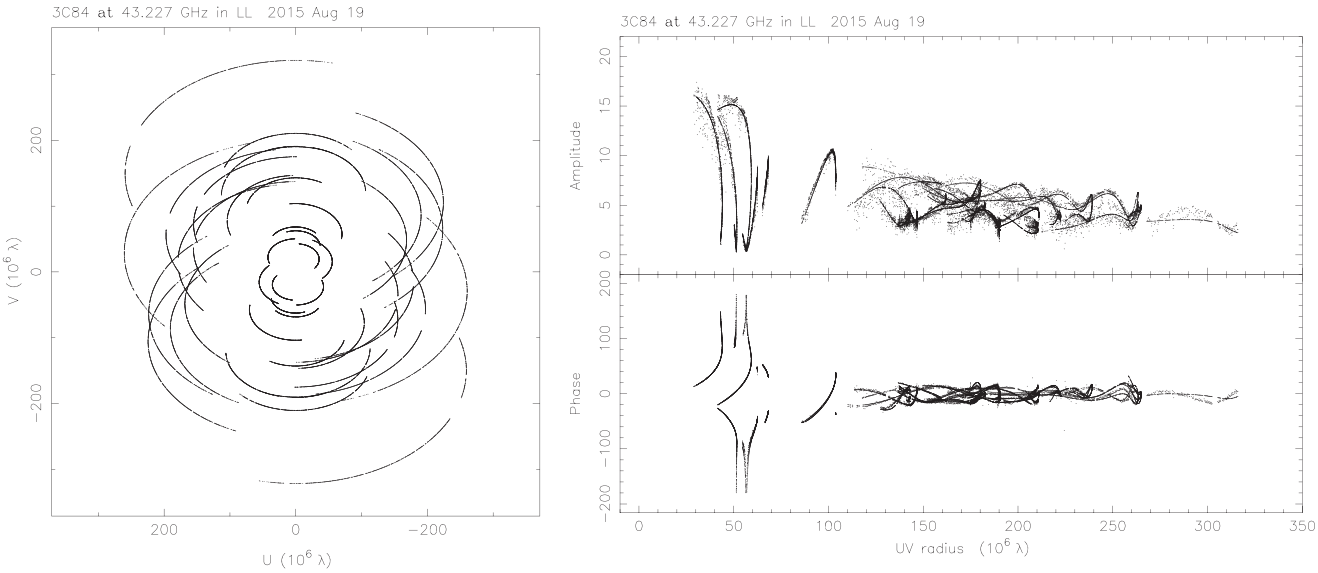

Figure 1. *uv* coverage, visibility amplitude, and phase obtained on 2015 August. This is one of the epochs during this KaVA monitoring of 3C 84 at 43 GHz.

In this work, we define the radio spectral index α_R as $S_\nu \propto \nu^{-\alpha_R}$. The cosmological parameters used here are as follows; $H_0 = 71\,\mathrm{km\,s^{-1}\,Mpc^{-1}}$, $\Omega_\lambda = 0.73$, and $\Omega_m = 0.27$ (e.g., Komatsu et al. 2011). The redshift of 3C 84 ($z = 0.018$) is located at the distance 75 Mpc and it corresponds to $0.35\,\mathrm{pc\,mas^{-1}}$. The mass of the BH in NGC 1275 is estimated to be around $M_\bullet \approx 8 \times 10^8\,M_\odot$ (Scharwächter et al. 2013) and we adopt this value. The corresponding Eddington luminosity is $L_{\rm Edd} \approx 1 \times 10^{47}\,\mathrm{erg\,s^{-1}}$. The normalized physical quantity is denoted as $Q = 10^x Q_x$, otherwise stated.

2. Observation and Data Reduction

From 2015 August to 2016 June, we conducted full-track 12-epoch monitoring of 3C 84 at 43 GHz with KaVA, the combination of the Korean VLBI Network (KVN) and the Japanese VLBI Exploration of Radio Astrometry (VERA) radio arrays. The joint array, KaVA, has a total of 7 antennas at frequencies of 22 and 43 GHz, resulting in angular resolutions of about 1.2 and 0.6 mas, respectively. The basic imaging capabilities of KaVA have been summarized in detail by Niinuma et al. (2014) and Hada et al. (2017). Left-hand circular polarization was received and sampled with a 2-bit quantization. All the data were recorded at 1 Gbps (256 MHz bandwidth, 16 MHz, 16 sub-bands) and correlated by the Daejeon correlator. On a technical note, we note that in the flux calibration of KaVA, visibility amplitudes correlated by the Daejeon hardware correlator (Lee et al. 2015b) should be corrected by multiplying by a factor of 1.35 (Lee et al. 2015a).

In Figure 1, we show the visibility amplitude and phase obtained in one of the KaVA monitoring epochs with typical data quality. The on-source time for 3C 84 was about 6–7 hr, which is sufficiently long for obtaining good *uv* coverage. The typical size of the original beam of KaVA at 43 GHz is 0.6–0.7 mas, and we restored all of the images with a beam size of 0.75 mas. In Table 1, we show the observation summary used in this work. As seen in the second column of Table 1, some stations were lost (marked with a minus sign) in some of the KaVA monitoring observations due to system troubles during some of the epochs. Three epochs of the images obtained by the Very Long Baseline Array (VLBA) in the framework of the Boston University (BU) Blazar monitoring program[8] are also included for consistency check purposes. We followed the standard procedures for initial phase and amplitude calibration using the National Radio Astronomy Observatories Astronomical Imaging Processing System (Greisen 2003). A priori amplitude calibration was applied using the measured system noise temperature and the elevation-gain curve of each antenna. We calibrated the bandpass characteristics of phase and amplitude at each station using the auto-correlation data. Following the amplitude calibration, fringe-fitting was performed to calibrate the visibility phases, and finally the data were averaged over each intermediate frequency band. The imaging and self-calibration were performed in the Difmap software (Shepherd 1997) in the usual manner.

3. Observational Results

3.1. Position of C3 Component

Let us estimate the positional accuracy of C3 relative to C1.[9] The peak positions of the C1 and C3 components are determined based on the standard model-fitting procedure in Difmap. First, we estimate a systematic error in position due to the positional scattering of the peak position of C1 from the origin point in the difmap during the period when the peak flux density of C1 is brighter than that of C3 (first half of our observation period). From the data, we obtained the positional scattering of C1 as about 0.02–0.07 mas. Second, we should estimate the systematic error. A deconvolution error is a known, major systematic error, and is possibly caused by some other component, such as the C2 component (e.g., Nagai et al. 2010). In our observation, however, the peak flux density of C3 ($\gtrsim$5 Jy) is more than a factor of ∼3 brighter than that of C2 (0.9–1.8 Jy) and the separation angle of C2 and C3 (∼2 mas) is larger than the beam size of KaVA at 43 GHz (∼0.6–0.7 mas). Therefore, it is clear that the deconvolution error by C2 is negligibly small. Third, note that a nominal estimate of the

[8] https://www.bu.edu/blazars/research.html

[9] Since we did not conduct a phase-referencing mode observation but a normal imaging one, the position of C3 is defined as a relative position to C1.

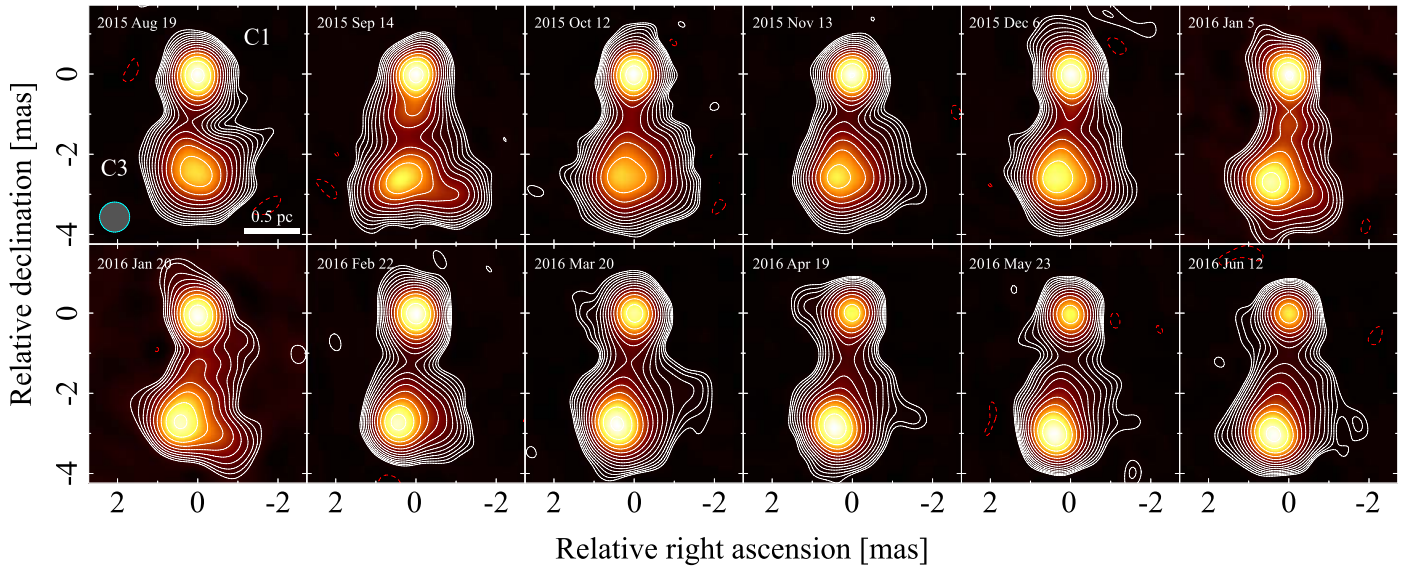

Figure 2. Multi-epoch KaVA images of 3C 84 at 43 GHz. The 12-epoch VLBI images of 3C 84 were obtained by KaVA at 43.2 GHz from 2015 August 19 (top left) to 2016 June 12 (bottom right). All images are restored with the circular Gaussian beam of 0.75 mas × 0.75 mas, which is indicated in the lower left corner of the first-epoch image. The lowest contour is three times the off-source rms noise (σ). The dashed and solid curves show negative and positive contours, respectively, and the contour levels are -3σ, $3\sigma \times (\sqrt{(2)})^n$ ($n = 0, 1, 2, ...$).

Table 1
Observation Summary

UT Date (MJD)	Stations	Image rms (mJy beam^{-1})	Peak Intensity (Jy beam^{-1})	Dynamic Range
2015 Aug 1	VLBA (Boston U. monitor)	0.90	6.00	6.70×10^3
2015 Aug 19 (57253)	KaVA	3.97	5.72	1.44×10^3
2015 Sep 14 (57279)	KaVA-MIZ, IRK, OGA	4.95	5.38	1.09×10^3
2015 Sep 22	VLBA (Boston U. monitor)	0.86	5.54	6.44×10^3
2015 Oct 12 (57307)	KaVA-IRK	3.56	4.94	1.39×10^3
2015 Nov 13 (57339)	KaVA-MIZ	10.21	4.92	4.80×10^2
2015 Dec 5	VLBA (Boston U. monitor)	0.97	5.27	5.43×10^3
2015 Dec 06 (57362)	KaVA	2.28	5.21	2.29×10^3
2016 Jan 05 (57392)	KaVA	3.49	5.18	1.48×10^3
2016 Feb 22 (57440)	KaVA-KUS	4.93	6.48	1.31×10^3
2016 Mar 20 (57467)	KaVA	2.60	7.84	3.02×10^3
2016 Apr 19 (57497)	KaVA	3.52	8.31	0.90×10^3
2016 May 23 (57531)	KaVA-MIZ	9.95	8.94	0.90×10^3
2016 Jun 12 (57551)	KaVA	6.67	9.80	1.47×10^3

position accuracy, i.e., the KaVA beam size divided by the dynamic range (a few 10^3), is much smaller than the systematic error from the peak position scattering of C1. Based on these error estimations, we conservatively set the positional accuracy of C3 relative to C1 as 0.07 mas. The error bars in the position in Figure 2 correspond to the 0.07 mas. Since both C1 and C3 are so bright, one can generally obtain a quite high positional accuracy of C3 relative to C1, which is clearly reflected in the high values of the dynamic ranges shown in Table 1.

For consistency, we have included three epochs of VLBA archival data from the BU Blazar monitoring program. The peak positions of C3 with VLBA (see the Appendix) are also shown in Figure 3 as triangles and these locations are consistent with those measured with KaVA.

Generally, one should be aware that C3 contains substructures (e.g., Nagai et al. 2014; Giovannini et al. 2018). When we discuss these substructures inside the C3 component, a higher spatial resolution is required because substructures cannot be resolved with the KaVA beam. In the present work, we focus on the kinematics of the spatially averaged positions of C3 and thus the KaVA beam size is sufficient for this investigation. We also confirm good agreements for spatially averaged positions in C3 between the KaVA and VLBA images shown in the Appendix.

In terms of structures around C3, we should also note a newly generated temporal structure shortly extending toward the West of C3 in the subsequent three epochs (2015 December 6th, 2016 January 5th, and January 20). We will briefly discuss a possible origin for this substructure in Section 5.2.

3.2. Flip of the C3 Component

In Figure 2, we show the 12-epoch images of 3C 84 at 43 GHz obtained with KaVA during the period from 2015 August to 2016 June. Here, we can see the overall propagation of the C3 component toward the south, and the change of the

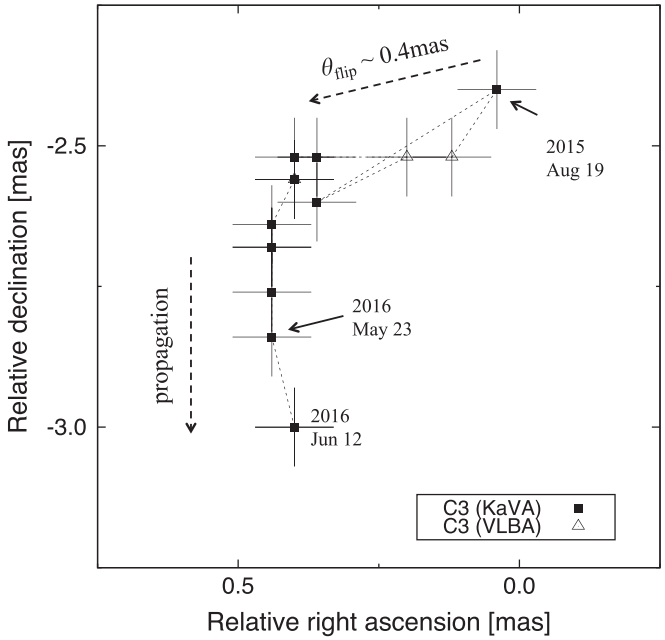

Figure 3. Relative peak intensity position of the component C3 with respect to C1 assuming (0,0) as an origin. The filled squares and open triangles represent the peak intensity positions obtained with KaVA and VLBA observations, respectively.

flux densities of the C1 and C3 components.[10] In Figure 3, we show the location of the peak position of the C3 component relative to the peak location of the C1 component. The C3 position on 2015 August 1 is well along the extended line of the past trajectory of C3 (Nagai et al. 2010; Suzuki et al. 2012; Hiura et al. 2018). As seen in Figure 3, we discover the flip of the C3 position during 2015 August–September. After 2015 September, all the epochs obtained with KaVA and VLBA show the flip of C3 in relative right ascension. As seen in Figure 2, the motion of the peak position of C3 was decelerated and C3 wobbled for a few months. After that, the peak position of C3 resumed propagating toward the south in the sky. Intriguingly, the apparent velocity of C3 temporally seems to reach a velocity comparable to c after 2015 September. Hence, Doppler boosting could potentially contribute to the brightening of C3 in the light curve. Since the number of observation epochs here is not enough to draw any conclusions, we will separately explore this issue in our forthcoming paper by adding further observation epochs from the period 2017–2018.

3.3. Light Curves of C1 and C3

In Figure 4, we show the light curves of the C3 and C1 components. The clear monotonic increase of the peak intensity of C3 is found in the overall trend of the light curve. The peak intensity of C3 increased by more than a factor of ∼4. On the other hand, the peak intensity of C1 does not show such a monotonic increase in the flux density and it was in the range of ∼5–6 Jy beam^{-1} during the observation period. The peak intensity of C3 finally exceeded that of C1 during winter of 2016. In the last epoch, i.e., 2016 June 12, the peak intensity of C3 became more than 4 Jy brighter than that of C1. As shown

[10] The apparent extended structure on the southwest side of the image in the 2015 September epoch in Figure 2 is not a real structure. It was an artifact from poorer *uv* coverage due to a lack of stations in KaVA at this epoch (see the second column of Table 1).

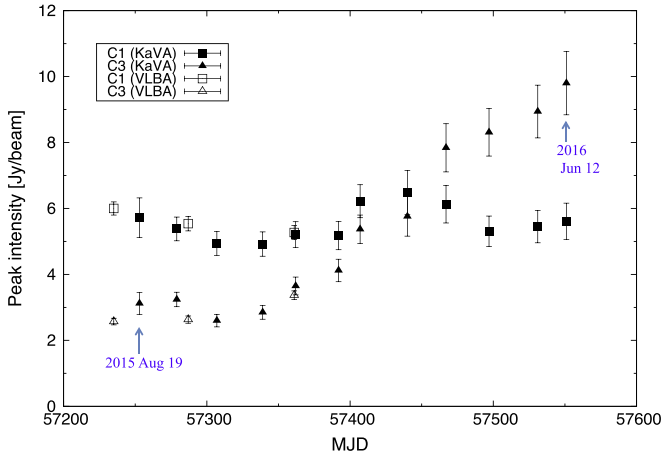

Figure 4. Light curve of the components C1 and C3 measured by KaVA and VLBA at 43 GHz from 2015 August to 2016 June. The filled and open points correspond to the peak intensity of C1 (square) and C3 (triangle) measured by KaVA and VLBA, respectively. All data points are obtained from the restored images shown in Figures 2 and 6.

in Figure 4 and Table 1, the peak flux density measured by VLBA on 2015 December 5th and the one measured by KaVA on 2015 December 6th show a good agreement with each other. This agreement of the independent VLBI arrays of KaVA and VLBA guarantees the robustness of the flux measurements of these two arrays.

It is noteworthy that the onset of the C3 flux density increase was seen at about MJD 57350. This means that the brightening of C3 was realized with a ∼100 day delay from the date of the flip around MJD 57250. As explained in Section 3.2, the propagation of C3 was suspended for a few months. After around MJD 57350, it resumed advancing southward. The onset of the C3 flux density increase coincides with this restart of the C3 propagation toward the south rather than the moment of the flip of C3.

4. Number Density of the Clump

To change the direction of jet propagation, there may be two possible mechanisms. One is the precession of a jet axis, and the other is a collision with obstacles. As for the precession, Falceta-Gonçalves et al. (2010) proposed a scenario in which the observed morphology of 3C 84 on 10–100 kpc scales can be explained by a precessing jet with a period of ∼10^7 years, using three-dimensional numerical simulations considering the jet precession evolution. Recently, an indication of the precession of the 3C 84 jet was reported by Hiura et al. (2018) based on VERA monitoring of 3C 84 at 22 GHz during the period of 2007–2013. The VERA data revealed that the relative position of C3 against C1 showed a smooth sinusoidal curve with a period of about 6 years, which can be explained by the jet precession. The relative position of C3 detected by KaVA during 2015 is reported in the present work; however, it is clearly different from the sinusoidal curve, with a flip and wobbling motion that can be naturally explained by a collision between the jet and a surrounding non-uniform/clumpy medium. The recent detection of the enhanced linearly polarized emission of the C3 component in 3C 84 was found in the same period and this enhancement can also support the interaction between the jet and clumpy medium (Nagai et al. 2017, see also Section 5). Because of these reasons, we assume

that the flip of C3 is caused by the dense clump and hereafter we estimate the number density of the clump.

If the 3C 84 jet thrust completely overwhelms the ram pressure by the clump, then the clump is dynamically negligible. Then the jet would continue to propagate along the same direction without any flip of the jet-head. On the other hand, a too dense clump would completely intervene with the jet propagations. To realize the flip of the jet-head, the jet thrust should be comparable to the ram pressure by the clump (e.g., a numerical simulation shown in Figure 6 of the paper Wang et al. 2000). From this condition, one can obtain

$$\frac{L_{\rm j}}{c} \approx \rho_{\rm cl} v_{\rm h}^2 A_{\rm cross}, \tag{1}$$

where $L_{\rm j}$, $\rho_{\rm cl}$, $v_{\rm h}$, and $A_{\rm cross} \equiv \pi (D_L \theta_{\rm flip})^2$ are the total kinetic power of the jet, the mass density of the clump, the jet-head advancing velocity and the effective cross-sectional area of the jet–clump interaction, respectively (Begelman & Cioffi 1989; Kino & Kawakatu 2005). In Section 5.2, we will present a consistency check for this assumption for Equation (1). According to recent VLBI observations, the averaged velocity of the jet after the emergence of the C3 component is known as

$$0.2\, c \lesssim v_{\rm h} \lesssim 0.3\, c, \tag{2}$$

(Nagai et al. 2010; Suzuki et al. 2012; Hiura et al. 2018). Here, we set the effective cross-sectional area as

$$A_{\rm cross} \approx 1.9\pi \times 10^{35} \left(\frac{\theta_{\rm flip}}{0.4\ {\rm mas}} \right)^2 {\rm cm}^{-2}. \tag{3}$$

In principle, the cross-sectional area of the clump $A_{\rm cl} \equiv \pi R_{\rm cl}^2$ can be larger than this effective cross-sectional one $A_{\rm cross}$ since there may exist a remaining part of the clump on the west side of the jet-head flip region. Hence, we introduce a numerical factor $\eta \equiv A_{\rm cl}/A_{\rm cross}$. Therefore, we take into account such cases and hereafter we mainly examine the case of $\eta \approx 1$. The corresponding radius of the clump ($R_{\rm cl}$) can be given by $R_{\rm cl} \approx 0.14 \eta^{1/2}$ pc. In Section 5.2, we will briefly address the case of $\eta \gg 1$ as well.

The total kinetic power of the jet $L_{\rm j}$ has also been constrained in the literature/. Heinz et al. (1998) argued that the time-averaged total power of the jet in NGC 1275 probably exceeds $L_j \sim 1 \times 10^{46}$ erg s^{-1}. They derived the conclusion based on the observed properties of X-ray cavities in the central region of the Perseus cluster, which is supposed to be inflated by the relativistic particles of the shocked jet. Hence, the minimum value of the jet power can be nominally $L_j \sim 1 \times 10^{46}$ erg s^{-1}.[11] As for the maximum value of L_j, Tavecchio & Ghisellini (2014) employed the largest jet power $L_j = 2.3 \times 10^{47}$ erg s^{-1} based on their model fitting against the non-thermal emission spectrum observed in 3C 84. This value suggested by Tavecchio & Ghisellini (2014) is comparable to $L_{\rm Edd}$. We adopt this value as the maximum value of L_j. Summing up, we set the range of L_j as

$$1 \times 10^{46}\ {\rm erg\ s} \lesssim L_{\rm j} \lesssim 2 \times 10^{47}\ {\rm erg\ s} \tag{4}$$

in the present work.

[11] However, they also suggested that the jet power in a quiescent state (corresponding to off-state mentioned in the paper of Reynolds & Begelman 1997) may be lower than $L_j \sim 10^{46}$ erg s^{-1}.

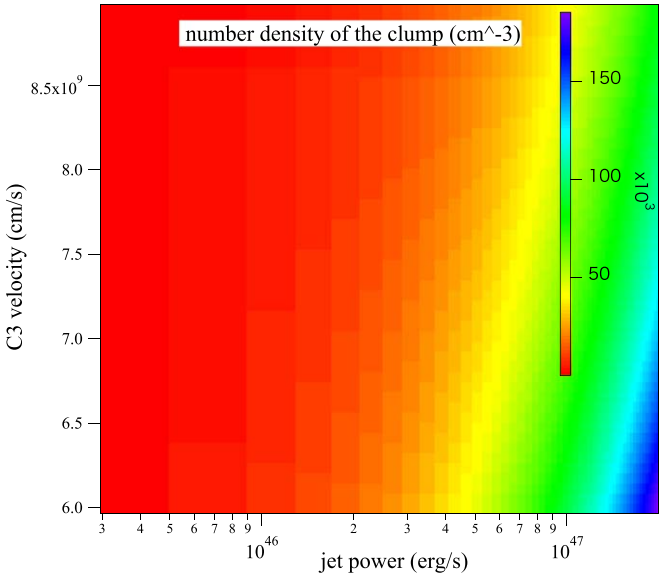

Figure 5. Estimated number density of the clump ($n_{\rm cl}$), based on Equation (1). The color contour indicates $n_{\rm cl}$ in units of 10^3 cm^{-3}. The vertical axis shows the advancing velocity of the C3 component ($v_{\rm h}$), while the horizontal axis represents the total jet power ($L_{\rm j}$).

In Figure 5, we show the estimated range of the clump density $n_{\rm cl}$ based on Equation (1), i.e., simply based on the momentum balance relation. By substituting the allowed values of $L_{\rm j}$ and $\rho_{\rm cl}$ shown in Equations (2) and (4), one can obtain the allowed value of $n_{\rm cl}$ and it is given by

$$4 \times 10^3\ {\rm cm}^{-3} \lesssim n_{\rm cl} \lesssim 2 \times 10^5\ {\rm cm}^{-3}. \tag{5}$$

The bottom right part of the allowed region in Figure 5 corresponds to the case of a denser clump, while the left side region represents the case of a thinner clump. We note that an enclosed total mass of the clump ($M_{\rm cl,obs} = 4\pi R_{\rm cl}^3/3$) can be estimated as $M_{\rm cl,obs} \approx 3\, M_\odot n_{\rm cl,4} (R_{\rm cl}/0.14\ {\rm pc})^3$.

5. Discussions

5.1. Origin of the Clump

In the previous section, we constrained the number density of the clump located 1 pc from the central engine of 3C 84 via the simple dynamical argument of jet–clump interaction. Here, we will discuss possible origins of the clump based on its location and number density. Since the typical density and location of a cloud in a broad line region (BLR; e.g., Osterbrock 1989; Peterson 1997; Maiolino et al. 2010; Bentz et al. 2013; Czerny et al. 2017) are obviously different from those for the clump in 3C 84, we will not further discuss the possibility of clouds in a BLR below.

5.1.1. A Cloud in a Narrow Line Region (NLR)?

Consider the possibility that a cloud in an NLR is the origin of the clump. A typical number density is $\sim 10^{2-5}$ cm^{-3} (e.g., Osterbrock 1989), thus a typical number density of cloud in NLR would agree well with the estimated number density of the clump ($n_{\rm cl}$) in 3C 84. In this sub-section, we further discuss whether the radial dependence of $n_{\rm cl}$ in 3C 84 has a similar trend with other AGN sources. Typically, NLR clouds in moderately luminous AGNs such as Seyfert galaxies are expected to be located in the broad radial range of 10^{1-3} pc

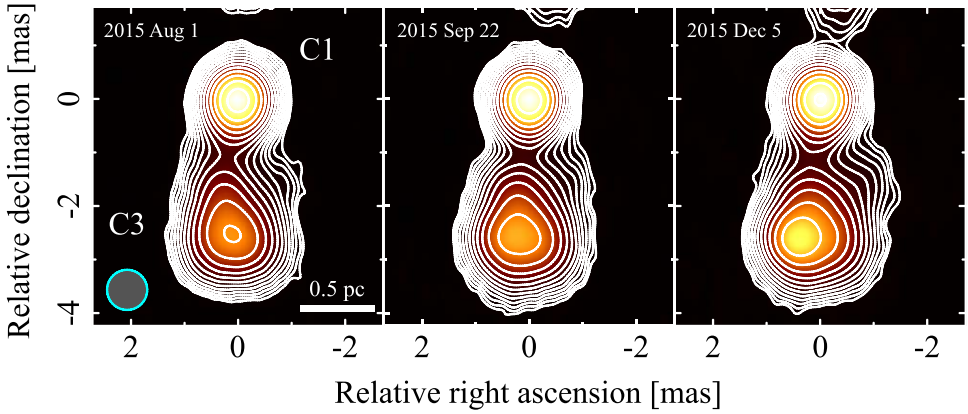

Figure 6. Three-epoch VLBI images of 3C 84 obtained by VLBA at 43 GHz from 2015 August 1 (left) to 2015 December 5 (right). All images are restored with the circular Gaussian beam of 0.75 mas × 0.75 mas, which is indicated in the lower left corner of the first-epoch image. The definitions of the curves and contour levels are identical to those in Figure 2.

from the central engine (e.g., Ramos Almeida & Ricci 2017). Some NLRs expand enough to be partially resolved on the sky (e.g., Pogge 1988; Tadhunter & Tsvetanov 1989; Schmitt et al. 1994; Fischer et al. 2013).

First, let us begin with an estimate of the size of NLR ($R_{\rm NLR}$) for NGC 1275. The $L_{\rm H\beta}$ luminosity is estimated by the luminosity of the Hα and Hβ emission line luminosities has the empirical relation of $3L_{\rm H\beta} \approx L_{\rm H\alpha}$ (Figure 5 in Greene & Ho 2005) and we have $L_{\rm H\alpha} \sim 1 \times 10^{42}\,{\rm erg\,s^{-1}}$ in NGC 1275 from a KANATA observation (Yamazaki et al. 2013; Kino et al. 2016). Therefore, the size of NRL in NGC 1275 can be estimated as $R_{\rm NLR} \approx 0.6 \times 10^2\,{\rm pc}\, L_{\rm H\beta,41}^{1/3} \epsilon_{\rm fill,-2}^{-1/3} n_4^{-2/3}$, where the filling factor of the NRL, and the number density of electrons are $\epsilon_{\rm fill}$, and n, respectively. The derived $R_{\rm NLR}$ value is comparable to typical values in other sources (e.g., Osterbrock 1989).

Next, let us compare the location and $n_{\rm cl}$ of the clump in 3C 84 with those in other AGN sources. Interestingly, Walsh et al. (2008) conducted imaging spectrograph observations of nearby low-luminosity AGNs with the Space Telescope Imaging Spectrograph (STIS) on board the the *Hubble Space Telescope* and they found that the electron number density measurements are characterized by a similar slope with a normalization of the electron number density of $5 \times 10^3\,{\rm cm^{-3}}$ at $\sim$1 pc from the core for five low-luminosity AGNs: NGC 1052, NGC 3227, NGC 3998, NGC 4278, and NGC 4579 (see Figure 7 in Walsh et al. 2008). Murayama & Taniguchi (1998) also indicated the radial dependence of the electron number density distribution in NLR via detection of coronal lines, which is known to be an indicator of denser clumps. Regarding the location of the clump, i.e., 1 pc from the central engine, Figure 7 of Walsh et al. (2008) indicates the electron number density as $n_{\rm cl} \sim 10^{3-5}\,{\rm cm^{-3}}$, which agrees with our estimate. Therefore, we conclude that the clump in 3C 84 can be understood as a cloud located deep inside (i.e., $\sim$1 pc) the NLR, with a normal number density.

5.1.2. A Self-gravitating Molecular Cloud?

As an alternative explanation that also agrees with the estimated $n_{\rm cl}$, here we discuss a case in which an intergalactic cloud such as a dark cloud, which is a circumstellar cloud with typical sizes, masses, and temperatures of 0.1–3 pc, $10^{2-7}\,{\rm cm^{-3}}$, and 10–100 K (Goldsmith 1987), is the origin of the clump. Interactions between galactic jet sources and such cold clumps are indeed suggested in some observations (e.g., Fukui et al. 2009). Here, we briefly discuss a case in which the clump is self-gravitating, since intergalactic molecular clouds are quite important in the context of star formation. The radius and mass of a self-gravitating clump in the context of AGNs have been estimated in the literature (e.g., Krolik & Begelman 1988; Hönig & Beckert 2007; Kawaguchi & Mori 2011) and we follow those arguments here. The two conditions required for self-gravitational clumps are as follows. The first requirement is that the freefall time for a spherical clump ($t_{\rm ff} = \sqrt{3\pi/(32\rho_{\rm cl}G)}$) be shorter than the sound crossing time ($t_{\rm crs} = R_{\rm cl}/c_s$). The second requirement is that these clump be stable against the tidal force in the gravitational field of the central BH ($F_{\rm tidal} \approx 2GM_\bullet M_{\rm cl}R_{\rm cl}/r^3$) by the self-gravity force ($F_{\rm sg} \approx GM_{\rm cl}^2/R_{\rm cl}^2$), where r is the distance from the central BH to the clump. The second requirement comes down to the relation $(R_{\rm cl}/r)^3 \lesssim M_{\rm cl}/2M_\bullet$. From these conditions, we have $R_{\rm cl} \lesssim \frac{\pi}{\sqrt{16G}}\frac{c_s r^{3/2}}{M_\bullet^{1/2}} \approx 1.6 \times 10^{-2} c_{s,5}(r/1\,{\rm pc})^{3/2}(M_\bullet/10^8\,M_\odot)^{-1/2}\,{\rm pc}$ and $M_{\rm cl,crit} = \frac{\pi^2 c_s^2}{8G}R_{\rm cl} \approx 0.5\,M_\odot c_{s,5}^3(r/1\,{\rm pc})^{3/2}(M_\bullet/10^8\,M_\odot)^{-1/2}$. From this, it is clear that the clump can become self-gravitating only when the clump is cold (i.e., slow sound speed of order of $c_s \lesssim 10^5\,{\rm cm\,s^{-1}}$), although there is no direct evidence of cold clumps in 3C 84 so far. Therefore, observational explorations of cold clumps are essential for testing this scenario. Cold gas is further discussed in Section 5.3.2.

5.1.3. A Giant Cloud?

Here, we briefly discuss the possibility of the existence of a clump with a cross-sectional area $A_{\rm cl}$ larger than that of $A_{\rm cross}$ (i.e., $\eta > 1$). If a giant molecular cloud larger than the few-parsec scale (Goldsmith 1987) known for our Galaxy exists, then NGC may be one of the possible candidates. The remaining part of such a large cloud would probably hold back on the western side of the radio lobe of the shocked material escaped from C3 and produce a remnant structure (see details in Section 5.2). Do we find such a remnant feature? Here, we speculate that the diffuse component C2 may be identical to the remnant of the exhausted jet produced by the interaction of the jet and a large clump. Although little attention

has been paid to C2, its existence is known in the literature (e.g., Venturi et al. 1993; Dhawan et al. 1998) and C2 does not show a systematic motion but does show a random wobbling behavior. Such a behavior could be explained by a collision with a large clump, which could cause a backflow of the exhausted jet (Asada et al. 2006; Mizuta et al. 2010). This scenario could be investigated using the high-energy γ-ray emissions caused by strong shocks (e.g., Kino & Asano 2011; Kino et al. 2017), although detailed investigations of such high-energy γ-ray spectra are beyond the scope of this paper.

5.2. Comparison with Hydrodynamical Simulations

In this sub-section, we will make comparisons of the observational results with hydrodynamical simulations of jet propagations in surrounding ambient matter.

5.2.1. Jet Confinement Condition in a Uniform Ambient Matter

First of all, it is important to check the availability of Equation (1) based on hydrodynamical simulations of jet propagations. To this end, simulations of jet propagations in a uniform ambient matter provide us a criterion for the availability of Equation (1). The propagation of a jet in a uniform ambient matter is essentially governed by the momentum balance between the jet thrust and the ram pressure from the ambient matter. Hence, the physical quantity L_j/n_a is the key to understanding the jet propagations where n_a is the number density of the ambient matter. It practically corresponds to the case of $\eta \gg 1$. Hereafter, we discuss the comparison of the obtained $n_{\rm cl}$ in 3C 84 with the hydrodynamical simulation of De Young (1993) by focusing on the quantity L_j/n_a. Let us begin with a brief summary of the hydrodynamical simulation of De Young (1993), who thoroughly examined the various combinations of L_j and n_a and investigated the condition of jet confinement by uniform ambient matter. They examined a case of jet propagations with total kinetic power $L_j \approx 1 \times 10^{45}$ erg s^{-1} and changing n_a and they found no jet confinement below $n_a \lesssim 3$ cm^{-3} (Figure 9 of De Young 1993). They also tested a case with $L_j \approx 1 \times 10^{44}$ erg s^{-1} in which the jet was still "confined" when $n_a \gtrsim 1.6$ cm^{-3} (Figure 9 of De Young 1993). Therefore, the condition for realizing jet confinement by a uniform ambient medium, based on the simulation of De Young (1993), can be written as

$$\frac{L_j}{n_a} \lesssim (6 \times 10^{43}\text{–}3 \times 10^{44})\ \text{erg cm}^3\ \text{s}^{-1}. \quad (6)$$

The estimate of $n_{\rm cl}$, together with the adopted L_j shown in Equation (4) in 3C 84 in the present work, shows a good agreement with the results of De Young (1993), i.e., the estimated upper limit of $L_j/n_{\rm cl}$ is almost the same as the criterion value inferred from the numerical results of De Young (1993). Thus, the flip of the jet-head of 3C 84 is well justified as a consequence of this jet–clump collision.

Note that the condition of confinement shown in Equation (6) is almost consistent with the work of Kawakatu et al. (2009), which showed that a hot spot, which corresponds to the reverse shock at the tip of the jet, is generated when

$$\frac{L_j}{n_a} \gtrsim 1 \times 10^{44}\ \text{erg cm}^3\ \text{s}^{-1}, \quad (7)$$

based on a Mach number value at the hot spot (termination shock) region.

5.2.2. A More Realistic Case: Inhomogeneous Ambient Matter

Next, we discuss the case of inhomogeneous ambient matter, which can provide insights for a more realistic situation. Wagner et al. (2012) took a comprehensive look at jet propagation in a two-phase ISM, which consists of warm and hot phases. The warm phase has a density perturbation and it produces clumps with an upper limit temperature of $\sim 10^4$ K. This situation qualitatively corresponds to the case of $\eta \sim O(1)$. In Wagner et al. (2012), no lower temperature limit was enforced and temperatures in the core of cloud (i.e., clump) could initially be less than 100 K. They found that the acceleration of the dense embedded clouds (clumps) is realized by the ram pressure of the high-velocity flow through the porous channels of the warm phase. This process transfers 10%–40% of the jet kinetic energy to the cold and warm gas, accelerating/blowing it to velocities that match those observed radio jets in AGNs. That is the so-called AGN feedback in mechanical energy form. The key feature seen in the simulation is a mixture of the flip of the jet-head and a blowout of clumps (Figure 9 of Wagner et al. 2012). Because of the significant non-uniformity of ambient matter, the dynamics of clumps cannot be purely determined by the head-on collision between the jet and a single clump alone. Perhaps such a hybrid case of jet flip and AGN feedback is more realistic in actual AGN jet sources. Wagner et al. (2012) showed that the AGN feedback is efficient for 10^{43} erg s$^{-1} \lesssim L_j \lesssim 10^{46}$ erg s^{-1}, with the number density of the clump as 30 cm$^{-3} \lesssim n_{\rm cl} \lesssim 10^3$ cm^{-3}. Since there is an overlap in these parameter ranges, we can expect a hybrid phenomenon in 3C 84. Indeed, as mentioned in Section 3.1, we detected a short-lived extended structure to the West of C3 from 2015 December to 2016 January. This structure has a substructure at the collision site between the jet and the clump, as demonstrated in Figure 9 of Wagner et al. (2012). As for the cloud/clump velocity, Wagner et al. (2012) predicted a typical velocity for the clumps after the collision as ranging from a few 100 to 1000 km s^{-1}. Therefore, this clump velocity will be one of the key observational quantities for testing the AGN feedback process in 3C 84 in the future.

5.3. Other Signatures of Clumpy Medium

Lastly, we briefly discuss other signatures of a clumpy medium in 3C 84.

5.3.1. Enhancement of Linear Polarization Emission

Nagai et al. (2017) recently reported the detection of significant polarized emission at the C3 component using VLBA observation data from the BU blazar monitoring program. Faraday rotation was also detected within an entire bandwidth of the 43 GHz band. The obtained rotation measure is $\sim 6 \times 10^5$ rad m^{-2} at maximum. Similar RM values were also reported at 210–345 GHz by Plambeck et al. (2014) using CARMA and SMA, while the 210–345 GHz emissions are likely to originate in the compact region at the close vicinity of the BH. Nagai et al. (2017) claimed that a simple spherical accretion flow cannot explain the RM observed with the VLBA and SMA/CARMA consistently. To reconcile it, Nagai et al. (2017) proposed a local clumpy/inhomogeneous ambient medium as being responsible for the

observed RM. When an equipartition condition between magnetic field and accreting gas holds, the electron density is estimated as $\sim 10^4\,\mathrm{cm}^{-3}$, which is comparable to the estimate of n_{cl} in this work. These results also strongly support the existence of the clump near the C3 component.

5.3.2. Searching for Cold Gas

Observationally, direct detections of cold gas within a 10 pc scale from central BHs are challenging and such explorations have just begun for other nearby active galaxies. In this context, Imanishi et al. (2018) made a first detection of cold gas on this scale (what they detected was a rotating dusty molecular torus) in the radio band using ALMA's high spatial resolution. First VLBI detection of HCN molecular absorption line features in NGC 1052 has been reported by Sawada-Satoh et al. (2016). We note that there are some detections of absorption lines by such clumps for ultra-luminous IR galaxies (e.g., Geballe et al. 2006; Sajina et al. 2009). We also note that a large fraction of X-ray-selected Seyfert 2 galaxies indeed show significant variations in the X-ray absorbing column density of N_{H} on a typical timescale of less than 1 year, which clearly suggests the presence of clumpy circumnuclear material on a scale below a parsec (Risaliti et al. 2002).

Although cold gas has not yet been detected at the circumnuclear region of NGC 1275, ALMA can potentially probe the cold molecular gas in the region. We proposed ALMA observations to study the morphological and kinematical properties of the cold molecular gas in the central few tens of parsecs (PI: H. Nagai), and the observations were partially completed. We also performed KVN observations to look for absorption lines caused by the cold molecular gas in the central few tens of parsecs (PI: K. Wajima). Such high-resolution observations toward NGC 1275 will definitely accelerate our understanding of the cold gas at the centers of nearby radio galaxies.

6. Summary

By performing multi-epoch monitoring observations with KaVA at 43 GHz in the period from 2015 August to 2016 June, we explored the kinematics of the notable newborn bright component C3 located at the tip of the radio jet 3C 84. We summarize our main findings as follows:

1. We discovered a flip of the peak position of the C3 component during 2015 August–September. The amount of positional shift in the angular scale was about 0.4 mas, which corresponds to 0.14 parsec in physical scale. After the flip, C3 wobbled at the same location for a few months and then it restarted propagating toward the south. For consistency check purposes, we have analyzed three epochs of VLBA archival data of 3C 84 at 43 GHz and the obtained position of C3 showed good agreement with those measured by KaVA.
2. We find a clear monotonic increase of the peak intensity of the C3 component during the observation period. The peak intensity of C3 increased by more than a factor 4 at the end of the observation period. On the other hand, the peak intensity of C1 remained almost constant within the range of 5–6 Jy beam^{-1} during the period. The flip of C3, together with this monotonic enhancement of its flux density, can be explained by a collision between the jet and a dense clump. The onset of the C3 flux density increase was seen at about MJD 57350, which does not coincide with the timing of the flip that happened around MJD 57250. The onset of the C3 flux density increase was coincident with the restart timing of the C3 propagation to the south rather than the moment of the flip of C3.
3. We estimate the density of the presumable clump based on the momentum balance between the jet thrust and the ram pressure from the clump and we find that the clump number density is estimated as about $4 \times 10^3\,\mathrm{cm}^{-3} \lesssim n_{\mathrm{cl}} \lesssim 2 \times 10^5\,\mathrm{cm}^{-3}$. The clump's location and estimated number density are in good agreement with a cloud located deep inside the NLR or a dense portion of an intergalactic molecular cloud.
4. The estimated value of L_j/n_{cl} for the jet–clump collision in 3C 84 satisfies the criterion for the jet confinement derived by the hydrodynamical simulation done by De Young (1993). It guarantees the availability of Equation (1) and the jet flip by the clump can be naturally expected. Further comparison with the hydrodynamical simulation by Wagner et al. (2012) provides us with predictions about more realistic cases of jet propagation in inhomogeneous ambient gas. Accelerations of clumps by the jet momentum can be realized through the porous channels in the inhomogeneous ambient gas. Since there is an overlap in the parameter ranges of Wagner et al. (2012), similar phenomena in 3C 84 may be expected. We will perform observations exploring such phenomena in the future.

This work is mainly based on observation with KaVA, which is operated by the the Korea Astronomy and Space Science Institute (KASI) and the National Astronomical Observatory of Japan (NAOJ). We thank K. Sugiyama for useful discussions. This work is partially supported by JSPS KAKENHI grants No. JP18K03656 (M.K.) and JP18H03721 (K.N., M.K., K.H.). N.K. acknowledges the financial support of MEXT KAKENHI (16K17670). H.N. is supported by MEXT KAKENHI grant No. 15K17619. This study makes use of 43 GHz VLBA data from the VLBA-BU Blazar Monitoring Program (VLBA-BU-BLAZAR; http://www.bu.edu/blazars/VLBAproject.html), funded by NASA through the Fermi Guest Investigator Program. VLBA is an instrument of the Long Baseline Observatory. The Long Baseline Observatory is a facility of the National Science Foundation operated by Associated Universities, Inc. This work was supported by the National Research Council of Science & Technology (NST) granted by the International joint research project (EU-16-001).

Appendix
VLBA Archival Data Analysis

For consistency, we used the VLBA archival data taken as a part of the BU Blazar Program. In Figure 6, we show the three-epoch images of 3C 84 at 43 GHz with all 10 VLBA stations (see also Table 1). The data consists of 4 intermediate frequencies (Ifs) with a 64 MHz bandwidth for each IF. The total bandwidth is 256 MHz per polarization. Both right-hand and left-hand circular polarizations were obtained. The data calibration procedure is the same as the one performed against KaVA data. Hence, we do not repeat it here. In order to compare the VLBA and KaVA images, we restore the VLBA images with the Gaussian beam size of 0.75 mas. The overall structures and fluxes obtained in the two epochs are consistent with those obtained by KaVA.

ORCID iDs

M. Kino https://orcid.org/0000-0002-2709-7338
K. Wajima https://orcid.org/0000-0003-3823-7954
H. Nagai https://orcid.org/0000-0003-0292-3645
G. Giovannini https://orcid.org/0000-0003-4916-6362
K. Hada https://orcid.org/0000-0001-6906-772X
K. Niinuma https://orcid.org/0000-0002-8169-3579
M. Giroletti https://orcid.org/0000-0002-8657-8852

References

Asada, K., Kameno, S., Shen, Z.-Q., et al. 2006, PASJ, 58, 261
Begelman, M. C., & Cioffi, D. F. 1989, ApJL, 345, L21
Bentz, M. C., Denney, K. D., Grier, C. J., et al. 2013, ApJ, 767, 149
Bicknell, G. V., Sutherland, R. S., van Breugel, W. J. M., et al. 2000, ApJ, 540, 678
Croton, D. J., Springel, V., White, S. D. M., et al. 2006, MNRAS, 365, 11
Czerny, B., Li, Y.-R., Hryniewicz, K., et al. 2017, ApJ, 846, 154
Dallacasa, D., Orienti, M., Fanti, C., Fanti, R., & Stanghellini, C. 2013, MNRAS, 433, 147
De Young, D. S. 1993, ApJ, 402, 95
Dhawan, V., Kellermann, K. I., & Romney, J. D. 1998, ApJL, 498, L111
Fabian, A. C. 2012, ARA&A, 50, 455
Falceta-Gonçalves, D., Caproni, A., Abraham, Z., Teixeira, D. M., & de Gouveia Dal Pino, E. M. 2010, ApJL, 713, L74
Fischer, T. C., Crenshaw, D. M., Kraemer, S. B., & Schmitt, H. R. 2013, ApJS, 209, 1
Fragile, P. C., Anninos, P., Croft, S., Lacy, M., & Witry, J. W. L. 2017, ApJ, 850, 171
Fukui, Y., Furukawa, N., Dame, T. M., et al. 2009, PASJ, 61, L23
Geballe, T. R., Goto, M., Usuda, T., Oka, T., & McCall, B. J. 2006, ApJ, 644, 907
Giovannini, G., Savolainen, T., Orienti, M., et al. 2018, NatAs, 2, 472
Goldsmith, P. F. 1987, in Interstellar Processes, Astrophysics and Space Science Library, Vol. 134, ed. D. J. Hollenbach & H. A. Thronson, Jr. (Dordrecht: Reidel), 51
Greene, J. E., & Ho, L. C. 2005, ApJ, 630, 122
Greisen, E. W. 2003, in Information Handling in Astronomy—Historical Vistas, Astrophysics and Space Science Library, Vol. 285, ed. A. Heck (Dordrecht: Kluwer Academic)
Hada, K., Park, J. H., Kino, M., et al. 2017, PASJ, 69, 71
Heinz, S., Reynolds, C. S., & Begelman, M. C. 1998, ApJ, 501, 126
Hiura, K., Nagai, H., Kino, M., et al. 2018, PASJ, in press (arXiv:1806.05302)
Hönig, S. F., & Beckert, T. 2007, MNRAS, 380, 1172
Imanishi, M., Nakanishi, K., Izumi, T., & Wada, K. 2018, ApJL, 853, L25
Ives, J. C., Sanford, P. W., & Penston, M. V. 1976, ApJL, 207, L159
Kawaguchi, T., & Mori, M. 2011, ApJ, 737, 105
Kawakatu, N., Kino, M., & Nagai, H. 2009a, ApJL, 697, L173
King, A. 2003, ApJL, 596, L27
Kino, M., & Asano, K. 2011, MNRAS, 412, L20
Kino, M., Ito, H., Kawakatu, N., et al. 2016, AN, 337, 47
Kino, M., Ito, H., Wajima, K., et al. 2017, ApJ, 843, 82
Kino, M., & Kawakatu, N. 2005, MNRAS, 364, 659
Komatsu, E., Smith, K. M., Dunkley, J., et al. 2011, ApJS, 192, 18
Krabbe, A., Sams, B. J., III, Genzel, R., Thatte, N., & Prada, F. 2000, A&A, 354, 439
Krolik, J. H., & Begelman, M. C. 1988, ApJ, 329, 702
Lee, S.-S., Byun, D.-Y., Oh, C. S., et al. 2015a, JKAS, 48, 229
Lee, S.-S., Oh, C. S., Roh, D.-G., et al. 2015b, JKAS, 48, 125
Lim, J., Ao, Y., & Dinh-V-Trung 2008, ApJ, 672, 252
Maiolino, R., Risaliti, G., Salvati, M., et al. 2010, A&A, 517, A47
Malizia, A., Bassani, L., Stephen, J. B., Malaguti, G., & Palumbo, G. G. C. 1997, ApJS, 113, 311
Mizuta, A., Kino, M., & Nagakura, H. 2010, ApJL, 709, L83
Murayama, T., & Taniguchi, Y. 1998, ApJL, 497, L9
Nagai, H., Fujita, Y., Nakamura, M., et al. 2017, ApJ, 849, 52
Nagai, H., Haga, T., Giovannini, G., et al. 2014, ApJ, 785, 53
Nagai, H., Suzuki, K., Asada, K., et al. 2010, PASJ, 62, L11
Niinuma, K., Lee, S.-S., Kino, M., et al. 2014, PASJ, 66, 103
O'Dea, C. P., Dent, W. A., & Balonek, T. J. 1984, ApJ, 278, 89
Orienti, M. 2016, AN, 337, 9
Orienti, M., & Dallacasa, D. 2014, MNRAS, 438, 463
Osterbrock, D. E. 1989, Astrophysics of Gaseous Nebulae and Active Galactic Nuclei (Mill Valley, CA: Univ. Science Books)
Peterson, B. M. 1997, An Introduction to Active Galactic Nuclei (Cambridge: Cambridge Univ. Press)
Plambeck, R. L., Bower, G. C., Rao, R., et al. 2014, ApJ, 797, 66
Pogge, R. W. 1988, ApJ, 328, 519
Ramos Almeida, C., & Ricci, C. 2017, NatAs, 1, 679
Reynolds, C. S., & Begelman, M. C. 1997, ApJL, 487, L135
Risaliti, G., Elvis, M., & Nicastro, F. 2002, ApJ, 571, 234
Sajina, A., Spoon, H., Yan, L., et al. 2009, ApJ, 703, 270
Salomé, P., Combes, F., Edge, A. C., et al. 2006, A&A, 454, 437
Sawada-Satoh, S., Roh, D.-G., Oh, S.-J., et al. 2016, ApJL, 830, L3
Scharwächter, J., McGregor, P. J., Dopita, M. A., & Beck, T. L. 2013, MNRAS, 429, 2315
Schmitt, H. R., Storchi-Bergmann, T., & Baldwin, J. A. 1994, ApJ, 423, 237
Shepherd, M. C. 1997, in ASP Conf. Ser. 125, Astronomical Data Analysis Software and Systems VI, ed. G. Hunt & H. E. Payne (San Francisco, CA: ASP), 125
Silk, J., & Rees, M. J. 1998, A&A, 331, L1
Sosa-Brito, R. M., Tacconi-Garman, L. E., Lehnert, M. D., & Gallimore, J. F. 2001, ApJS, 136, 61
Suzuki, K., Nagai, H., Kino, M., et al. 2012, ApJ, 746, 140
Tadhunter, C., & Tsvetanov, Z. 1989, Natur, 341, 422
Tavecchio, F., & Ghisellini, G. 2014, MNRAS, 443, 1224
Venturi, T., Readhead, A. C. S., Marr, J. M., & Backer, D. C. 1993, ApJ, 411, 552
Wagner, A. Y., & Bicknell, G. V. 2011, ApJ, 728, 29
Wagner, A. Y., Bicknell, G. V., & Umemura, M. 2012, ApJ, 757, 136
Walker, R. C., Dhawan, V., Romney, J. D., Kellermann, K. I., & Vermeulen, R. C. 2000, ApJ, 530, 233
Walsh, J. L., Barth, A. J., Ho, L. C., et al. 2008, AJ, 136, 1677
Wang, Z., Wiita, P. J., & Hooda, J. S. 2000, ApJ, 534, 201
Wilman, R. J., Edge, A. C., & Johnstone, R. M. 2005, MNRAS, 359, 755
Yamazaki, S., Fukazawa, Y., Sasada, M., et al. 2013, PASJ, 65, 30